LA-UR-19-28650 (Accepted Manuscript)

Novel design and diagnostics improvements for increased production capacity and improved reliability at the Los Alamos Isotope Production Facility

O'Brien, Ellen Margaret; Baily, Scott A.; Birnbaum, Eva R.; Chapman, Catherine A. B; Espinoza, Everett A.; Faucett, John Allen; Hill, Jeffrey Owen; John, Kevin Dale; Marroquin, Pilar Sotero; Mccrady, Rodney Craig; Norman, Deborah E.; Nortier, Francois Meiring; O'Hara, James Francis; Olivas, Eric Richard; Patten, Austin Randall; Pieck, Martin; Rybarcyk, Lawrence John; Snyder, Joseph Frank; Swensen, Erik Arnold; Valicenti, Raymond A.; Vermeulen, Christiaan; et al.

Provided by the author(s) and the Los Alamos National Laboratory (2020-01-03).

To be published in: Nuclear Instruments and Methods in Physics Research Section A: Accelerators, Spectrometers, Detectors and Associated Equipment

DOI to publisher's version: 10.1016/j.nima.2019.163316

Permalink to record: http://permalink.lanl.gov/object/view?what=info:lanl-repo/lareport/LA-UR-19-28650

Disclaimer:
Los Alamos National Laboratory, an affirmative action/equal opportunity employer, is operated by Triad National Security, LLC for the National Nuclear Security Administration of U.S. Department of Energy under contract 89233218CNA000001. By approving this article, the publisher recognizes that the U.S. Government retains nonexclusive, royalty-free license to publish or reproduce the published form of this contribution, or to allow others to do so, for U.S. Government purposes. Los Alamos National Laboratory requests that the publisher identify this article as work performed under the auspices of the U.S. Department of Energy. Los Alamos National Laboratory strongly supports academic freedom and a researcher's right to publish; as an institution, however, the Laboratory does not endorse the viewpoint of a publication or guarantee its technical correctness.

Journal Pre-proof

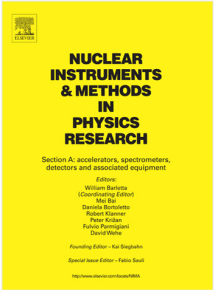

Novel design and diagnostics improvements for increased production capacity and improved reliability at the Los Alamos Isotope Production Facility

E.M. O'Brien, S.A. Baily, E.R. Birnbaum, C. Chapman, E.A. Espinoza, J.A. Faucett, J.O. Hill, K.D. John, P.S. Marroquin, R.C. McCrady, D.E. Norman, F.M. Nortier, J.F. O'Hara, E.R. Olivas, A.R. Patten, M. Pieck, L.J. Rybarcyk, J.F. Snyder, E.A. Swensen, R.A. Valicenti, C. Vermeulen, H.A. Watkins, K.A. Woloshun

PII: S0168-9002(19)31557-8
DOI: https://doi.org/10.1016/j.nima.2019.163316
Reference: NIMA 163316

To appear in: *Nuclear Inst. and Methods in Physics Research, A*

Received date : 26 August 2019
Revised date : 30 October 2019
Accepted date : 17 December 2019

Please cite this article as: E.M. O'Brien, S.A. Baily, E.R. Birnbaum et al., Novel design and diagnostics improvements for increased production capacity and improved reliability at the Los Alamos Isotope Production Facility, *Nuclear Inst. and Methods in Physics Research, A* (2019), doi: https://doi.org/10.1016/j.nima.2019.163316.

This is a PDF file of an article that has undergone enhancements after acceptance, such as the addition of a cover page and metadata, and formatting for readability, but it is not yet the definitive version of record. This version will undergo additional copyediting, typesetting and review before it is published in its final form, but we are providing this version to give early visibility of the article. Please note that, during the production process, errors may be discovered which could affect the content, and all legal disclaimers that apply to the journal pertain.

© 2019 Published by Elsevier B.V.

Journal Pre-proof

*Manuscript
Click here to view linked References

Novel Design and Diagnostics Improvements for Increased Production Capacity and Improved Reliability at the Los Alamos Isotope Production Facility

E.M. O'Brien[1a], S.A. Baily[a], E.R. Birnbaum[a], C. Chapman[a], E.A. Espinoza[a], J.A. Faucett[a], J.O. Hill[a], K.D. John[a], P.S. Marroquin[a], R.C. McCrady[a], D.E. Norman[a], F.M. Nortier[a], J.F. O'Hara[a], E.R. Olivas[a], A.R. Patten[a], M. Pieck[a], L.J. Rybarcyk[a], J.F. Snyder[a], E.A. Swensen[a], R.A. Valicenti[a], C. Vermeulen[a], H.A. Watkins[a], K.A. Woloshun[a]

[a]Los Alamos National Laboratory, P.O. Box 1663, Los Alamos, NM 87545 USA

ABSTRACT

The Isotope Production Facility (IPF) at Los Alamos National Laboratory (LANL) is used to produce an array of isotopes for medical, global security, and research applications with an intense beam of protons supplied by the linear accelerator at the Los Alamos Neutron Science Center (LANSCE). An Accelerator Improvement Project (AIP) was recently conducted at IPF to improve facility reliability and reduce programmatic risk while increasing general isotope production capacity and flexibility. This was accomplished through the installation of an improved beam window assembly, more robust beam diagnostics, an active and adjustable collimator, and a new beam rastering system. This paper will highlight the four exciting innovations and how they were designed, validated, and installed in parallel as well as the significant operational advantages they provide to IPF. Key experiments and the increased currents achieved in routine production runs demonstrating the enhanced capability from the AIP will be presented. The most notable capability enhancements include irradiations with beam currents ranging from 100 nA experimental runs up to 300 μA on routine production targets and utilization of a range of cylindrical target diameters.

Keywords

100 MeV protons, Active and adjustable collimator, Accelerator beam diagnostics, Accelerator improvement project, Beam rastering, Isotope Production Facility

1 INTRODUCTION

Initially commissioned in 2004, the Isotope Production Facility (IPF) is located at the Los Alamos Neutron Science Center (LANSCE) at Los Alamos National Laboratory (LANL) and is capable of producing a variety of radioisotopes utilizing proton energies up to 100 MeV [1]. The delivery of protons to a target stack through a dedicated beamline allows for beam transport, beam rastering, and beam diagnostics close to the targets. The target stack is separated from beamline vacuum via a semi-permanent beam window installation. Since the initial design and commissioning of this facility, several key areas have been pinpointed in which facility performance and reliability could be improved.

With the main motivations of improving facility reliability, reducing programmatic risk, and allowing for more production flexibility for either an increase in total production capacity and/or the ability to accommodate a wide array of R&D irradiations, an Accelerator Improvement Project (AIP) was funded by the Department of Energy Isotope Program and conducted at IPF between 2015 and 2017. The majority of this work was performed by LANL's Accelerator Operations & Technology (AOT) division, which encompasses a diverse group of expertise and is responsible for operating, maintaining, and enhancing the accelerator.

The improvement project consisted of four main components. The first one focused on reducing programmatic risk by redesigning, testing, validating, and installing a new and more robust beam window

[1] Corresponding author.
E-mail address: emobrien@lanl.gov (E.M. O'Brien)

Journal Pre-proof

assembly. The second component increased the previous beam rastering capabilities to enable optimized beam power distribution. The third project component improved beam diagnostic capabilities to more accurately predict the beam spot size, distribution, primary energy, and alignment at the target window. Both the beam diagnostic and the beam raster system project components were aimed at improving the reliability of operations at IPF by providing more information about the behavior of the incident proton beam. The beam raster system was also intended to provide a much more uniform beam power deposition across the target via the use of multi-circle raster patterns. The fourth project component involved the installation of an active and adjustable collimator capable of providing real-time diagnostic feedback on the incident beam spill, including nominal temperature measurements of the collimator sectors. The novel adjustability feature of the collimator enables the use of cylindrical targets of different diameters to facilitate increased production via the use of larger targets combined with higher beam intensity as well as allow for smaller targets that may be desired for R&D irradiations.

Key irradiations have demonstrated the enhanced capability from the AIP. Routine production target stacks are now operated at a nominal beam current of 250 μA with the enhanced raster, an ~8.7% increase from pre-AIP production currents. Metal targets (rubidium and gallium) have been demonstrated to 265 μA, with a commensurate increase in yields. The largest collimator aperture diameter has been actuated for the successful irradiation of 2.5 inch diameter RbCl and Ga targets at 300 μA, relative to the previous standard of 2 inch diameter targets. Low beam intensities of 100 nA were successfully utilized to irradiate foils for high fidelity nuclear data measurements.

2 BEAM WINDOW

The beam window at IPF is a semi-permanent installation with an expected lifetime of approximately 5-8 years based on historical integrated beam currents and acceptable window dose limits. The newly installed beam window was manufactured from annealed Inconel alloy 718 and its main purpose is to separate the beamline vacuum from the water-cooled target station, transmitting high intensity proton beams directed onto the production targets. As the facility plans to increase its nominal beam current from 230 μA towards 450 μA, it was desirable to decrease facility risk by improving the thermal performance and survivability of the beam window. In this respect, the installation of this new beam window design enables operation with a larger collimator aperture size, more elaborate raster patterns, and at a higher beam current.

A lifetime plastic deformation of approximately 0.15 cm was observed in the previous flat IPF beam window design, causing the beam window to progressively curve into the vacuum tube [2]. This curvature was a result of the differential pressure between the water-cooled target station and the vacuum beamline of an order exceeding the elastic limit of the Inconel combined with localized thermal stress from the proton beam heating. These factors caused high circumferential stresses at the intersection of the sharp edge of the heavier flange that secures the beam window. The beam window deformation has a direct influence on the thickness of the first cooling channel and thus the flow field behind the beam window. This observed deformation of the previous beam window was one of the predominant drivers influencing the beam window redesign.

A comprehensive parametric study was conducted to assess and optimize beam window survivability by varying beam size, incident beam energy, and beam intensity. Four case studies were conducted, and are listed in the table below. Each of these studies were performed for window thicknesses of 0.635, 0.508, 0.381, and 0.254 mm.

Table 1. Four case studies conducted on the proposed beam window designs with various thicknesses.

Collimator Aperture [cm]	Proton Energy [MeV]	Beam Current [μA]
5.84 (2.3 in)	41.3	300
3.56 (1.4 in)	100	300
5.84 (2.3 in)	100	450
3.56 (1.4 in)	41.3	450

Before performing the parametric study, to ensure the material quality and properties of the annealed Inconel alloy 718 intended for the new beam window were used in the model, strength tests were performed on the lot of Inconel sheets intended for the new beam window by an independent contractor. These strength test results set the boundary conditions for the simulations in order to determine if the beam window would survive in each case. These tests also ensured that the material used in both the installed beam window and the spare that was simultaneously manufactured exhibited yield strength performance consistent with the reference published data for this annealed Inconel alloy.

The parametric study was done by performing a computational fluid dynamic (CFD) simulation with input provided by a Monte Carlo N-Particle Transport Code (MCNP) generated power distribution of a three-circle rastered beam [3]. The results of this CFD simulation were then provided as input to a conjugate heat transfer (CHT) model to predict temperature and thermal stress distributions in the beam window. The assumed beam profile is shown in Figure 1.

Figure 1 Location

CHT models describe the thermal interaction between solids and the thermal hydraulic characteristics of fluids. The CHT solution was then supplied to a Finite Element (FE) model to predict the thermal mechanical stress and deformation based on the window temperature profile and the applied structural loads. This allowed for determination of the limiting conditions on overall beam window operation and health as well as optimization of the beam window thickness and shape.

Simulations indicate the safe operation of the beam window at a 3.56 cm (1.4 in) aperture size and 300 μA and at aperture sizes of 4.57 cm (1.8 in) – 5.84 cm (2.3 in) at 450 μA. For these cases the calculated temperatures, stresses, and deformation seen were well within acceptable limits for the Inconel alloy used in the beam window fabrication. It should be noted that potential beam window failure was predicted in the 3.56 cm (1.4 in) collimator aperture diameter, 41.3 MeV, 450 μA cases for all beam window thicknesses, creating a limiting operating condition.

ANSYS CFX and ANSYS Mechanical were used for the thermal hydraulic and structural analyses, respectively [4,5]. The results of the thermal hydraulic and mechanical analyses for the 0.381 mm thick beam window, 5.84 (2.3 in) collimator aperture size, and 100 MeV, 450 μA incident proton beam case are shown in Figures 2 and 3.

Figure 2 Location

Figure 3 Location

Based on the results of this parametric study, the redesigned beam window is now thinner, reduced in thickness from 0.635 mm to 0.381 mm, and is pre-curved by 1.27 mm in the center towards the vacuum side of the beamline. A drawing of this new preformed beam window is shown in Figure 4.

Figure 4 Location

The preformed beam window was produced via a stamping technique and then electron beam welded to the 304 stainless steel weld flange and adaptor. The beam window and weld flange are shown alongside the full beam window assembly in Figure 5.

Figure 5 Location

Due to the reduction in beam window thickness the power deposition, volumetric heating, and peak temperatures in this new window are considerably lower than the old window design.

The predicted thermal performance improvement of this new beam window design allows acceptance of beam currents in excess of 450 μA, although beam delivery is currently only authorized up to 380 μA. In addition, the beam window's design accommodates both a larger aperture size and more raster circles, enabling an increase in production volume.

2.1 Beam Window Displacement Measurement

A non-contact beam window displacement measurement device was developed in order to track any beam window deformation over time. The device is a stand-alone data logger that utilizes an eddy-current sensor to provide high-resolution non-contact displacement sensing over small distances. The data logger records data at a rate of 4 Hz and measures the beam window deflection with micrometer precision. The displacement measurement device is mounted inside of a plastic housing unit that allows for its attachment to the target stack trolley, as shown in Figure 6. Once the device is attached to the IPF trolley it can be lowered down the transfer tube to the beam window.

Figure 6 Location

In order to verify that the beam window deforms as expected under hydrostatic loading from the cooling water, benchtop testing was done using the displacement measurement device to monitor the deformation of a test beam window under pressure loading conditions from 0.1379 MPa (20 psig) – 0.4826 MPa (70 psig). At each hydrostatic loading pressure, at least 80 data points were recorded with the data logger in order to observe if there was any drift in the measured values. The set up configuration for this test is shown in Figure 7 for both the computer-aided design (CAD) model and experimental benchtop apparatus.

Figure 7 Location

The beam window deformation recorded by the data logger was compared with the results of an ANSYS Finite Element (FE) model. There was excellent agreement between the computational and experimentally measured values, indicating that the new beam window was deforming as expected. This test also verified that the displacement measurement device was functioning properly and that the beam window's response to the range of loading pressures was fully in the elastic deformation region.

This device should be able to observe any measurable plastic deformation in the beam window over time by taking these measurements every year. By recording the beam window position both with and without differential pressure, it is possible to observe the elastic rebound of the beam window and any plastic deformation over time. These measurements have been performed in the configuration shown in Figure 6 a total of three times – once after commissioning of the beam window and two times since then after two run cycles at IPF. Thus far the beam window appears to outperform its previous counterpart in terms of deformation, however, these measurements are ongoing and will continue for the duration of the beam window's lifetime. This tracking of any plastic deformation through deflection measurements also reduces the risk of future catastrophic beam window failure.

3 BEAM RASTERING

The beam raster system at IPF was upgraded in order to provide optimal heat distribution profiles for a range of target diameters to take advantage of the aperture variability of the active and adjustable collimator (described in Section 5). While the previous system generated a single circle, the new raster system is capable of producing up to 100 concentric circles in successive macropulses. The beam is rastered at a rate of 5 kHz by orthogonal raster magnets, with one complete raster cycle performed in 202 μs, leading to slightly more than three rotations per 625 μs macropulse. For each macropulse the revolutions are of the same diameter [6].

The circular raster patterns are achieved by synchronization of the master power supplies for the horizontal and vertical raster magnets in the IPF beamline with a nominal phase offset of 90°.

The beam rastering system is remotely controllable via a computer interface, and the system is capable of intra-day adjustments to account for daily variations in the beam spot size. This is done via independent adjustment of the horizontal and vertical amplitudes up to ±10% of the nominal value in 1% increments.

Current operations have utilized both three and five concentric circle raster patterns in a specifically optimized macropulse order to minimize peak power deposition. The burn marks for both a three-circle and five-circle raster pattern on a polymer film are shown in Figure 8. As the collimator segments begin to close, they overlap and no longer form a perfect circle, clipping the beam into the slightly rectangular shape observed in the three-circle raster burn mark. This is more pronounced at smaller aperture sizes.

Figure 8 Location

The raster system has two distinct equipment protection systems. They are the run permit and the fast protect systems. The run permit requires a certain set of safe configuration criteria to be met before the beam may be turned on. These criteria include set points on such parameters as the raster magnet temperatures, the magnet rastering power supplies, and water flow through the raster magnets. The fast protect system interrupts beam operation in the event of one of a number of abnormal beam conditions that could adversely affect the system, the beam window, or the target stack [6].

Because the run permit has an inherent response time on the order of tens of ms and is therefore unable to interrupt the beam in the event of abnormal beam conditions, the fast protect system protects the beam window by ensuring beam shut-off within 200 μs, or approximately one third of the way into one macropulse. This shut-off time is dictated by the thermal response time predicted by a thermal-mechanical worst-case scenario model with a 41.3 MeV, 450 μA unrastered beam and the smallest collimator aperture setting. Based on this worst-case scenario, beam delivery limits are set to ensure that the maximum beam window temperature remains below 200 °C. This ensures that the fast protect system achieves the necessary level of protection during operation in a worst-case scenario.

Prior to and during beam delivery, a redundant system checks that the delivered raster pattern is the one requested. If it deviates from this, e.g. a single unrastered spot versus a three-circle raster pattern, then the beam will turn off to ensure there is no damage to the beam window or target stack. This deviation is determined by comparing in real time the scheduled raster magnet's voltages and currents at the desired raster pattern with the measured values. Additional safety interlocks exist within the fast protect system to check for abnormal beam delivery conditions, such as a phase offset other than the one expected between the vertical and horizontal Alternating Current (AC) waveforms. These safety interlocks reduce the risk of damage to the beam window, target stack, or station due to off-normal incident beam.

The improved heat profile provided by the upgraded raster system allows for operation at higher beam currents and larger raster circle diameters as seen when operating with both the three- and five-circle raster patterns. The enhanced raster system enables an increase in production volume, higher isotope yields due to the larger target size and increased beam currents, and more versatility for R&D irradiations utilizing the smaller aperture size.

4 BEAM DIAGNOSTICS

The installation of both new and upgraded diagnostic devices in the form of an upgraded harp, new emittance slits, and a new wire scanner enables improved measurement capabilities and overall better prediction of the beam size, profile, and position, therefore enhancing the reliability of IPF and improving beam characteristics for maximum production. These tools also required the installation of new motion control and data acquisition electronics and equipment.

Upgrades to the IPF beamline that will be discussed in this section are indicated on the three-dimensional model and two-dimensional drawing of the IPF beamline in Figure 9 for perspective on their location.

Figure 9 Location

These installations reduce the probability of target failure due to improper visualization of the beam on the face of the target by providing additional feedback to the accelerator operators when tuning beam parameters.

4.1 High-Density Harp

An upgraded multi-wire beam profile device in the form of a high-density harp was installed to serve as both a beam profile measurement in two transverse directions (vertical and horizontal) and as a collector for emittance measurements. The emittance collection functionality will be described in detail later in Section 4.1.1. The harp was installed at a location just upstream of the beam window/collimator assembly to provide as accurate a picture of the beam profile incident on the target stack as possible.

The two orthogonal harp heads were designed to provide a 7.6 cm wide beam profile with a resolution of 1 mm. This was an improvement from the 2.4 mm spacing on the previous harp. To obtain this resolution, a harp head assembly requires 77 0.079 mm thick silicon carbide (SiC) wires. This resolution was implemented by employing a two-sided printed circuit board with the SiC wires spaced 2 mm apart on each side with a 1 mm offset between them. This spacing allows for the placement of approximately 49 of the 77 SiC wires within the beam spot-size envelope of $2\sigma = 4.8$ mm [7,8]. A physical harp head assembly and a three-dimensional CAD model of a harp head assembly and associated actuator design are shown in Figure 10.

Secondary charged particles in the form of electrons produced in the wires are correlated to a normalized measurement of beam intensity as a function of position, i.e. a profile. The secondary particle signals induced in the sensors travel along the harp circuit board's traces through the external wiring harness to the analog-to-digital convertors (ADCs). The harp is able to synchronously sample the beam profile every 10 μs over the duration of the macropulse. This feature enables measurements of either static or rastered beam profiles at low duty factor.

Figure 10 Location

The high-density harp was utilized in an experimental R&D run to visualize the beam distribution in both the horizontal and vertical directions and reposition accordingly in order to perform high fidelity nuclear data measurements with thin foils.

4.1.1 Emittance Measurement

The emittance measurement is a new addition to the IPF beamline and enables transverse phase-space-like measurements in the horizontal and vertical planes. The measured emittances are used directly in a beam envelope tune-up code to establish the beamline quadrupole magnet operating set points that will produce the desired unrastered beam spot at the target or elsewhere in the beamline. The measurement system requires both the newly upgraded harps, as the collectors, and the newly installed slits, located upstream of the harp, to make the correlated scans of position and divergence. The measured emittances also provide details about the beam distribution that are not available through simple root mean square (rms) reconstruction techniques and can facilitate more detailed analysis of the beam spot on the collimators, window, or target.

The slits were designed to provide high-resolution measurements and survive the power deposition of the 100 MeV, low duty-factor beam during a scan. The water-cooled copper slits have a 0.508 mm aperture size to limit the spatial averaging of the sample beam and a 14 mm thickness to absorb the 100 MeV incident beam and enhance the heat transfer. The slit geometry allows for a relatively high-resolution emittance scan relative to the beam spot size of $2\sigma = 4.8$ mm, while simultaneously minimizing slit-induced scattering. Two orthogonal slits are installed, their thickness chosen to fully absorb 100 MeV intercepted beam not passing through the slit. A visualization of the model for the emittance slit and actuator design is shown in Figure 11. The new system also required synchronized motion of each high-density harp head and emittance slit pair during a measurement. The high sample rate of the high-density harps in conjunction with the new emittance slits allows for the performance of time-dependent beam

profile and emittance measurements of the IPF beam. An example of the vertical IPF beam emittance measured on the high-density harp is shown in Figure 12.

Figure 11 Location

Figure 12 Location

4.2 Wire Scanner

As part of the beam monitoring upgrades, a new wire scanner was installed. This wire scanner has a 1 mm step size, a ~4.3 cm aperture size, and a ~20 cm linear stroke size. This stroke length is required to fully traverse the beam and be extracted from the ~10 cm diameter section of beam pipe in which it is located. The three-dimensional rendering of the wire scanner and actuator model design is shown in Figure 13.

Figure 13 Location

The wire scanner provides a higher resolution visualization of the beam profile in the horizontal and vertical directions when compared with the harp. It consists of a single wire in both the horizontal and vertical directions that is moved to provide a transverse beam profile scan with up to 10 μm resolution. It involves the movement of a thin wire quickly across the beam, causing a secondary particle shower that is then used to determine the magnitude of the beam profile at the traversed locations. The position and secondary particle shower signal are recorded simultaneously and then provided as a scanned image of the beam profile. These wire scanner profiles can be used in conjunction with simultaneously measured harp profiles to ascertain the rms beam emittance when used with the standard quadrupole scan (quad-scan) technique [9]. This can also be used in the beam envelope codes during beamline tune-up activities.

4.3 Beam Current Measurements

Prior to the AIP, beam current measurements below approximately 500 nA were unreliable, with large associated uncertainties. The upgraded beam current measurement system was designed for measurements of average beam currents ranging from 100 nA to 450 μA with 1% accuracy or better. The system was assumed to have a 1 mA peak minimum, a minimum frequency of 1 Hz, and a minimum pulse width of 100 μs.

These system performance criteria were met using the two pre-existing current monitor toroids indicated in Figure 9 and using existing preamp electronics. A new low average current device was designed to amplify the existing transimpedance preamp signal, digitize it using an advanced reduced instruction set computing (RISC) Machine (ARM) Cortex M4, and output digital current values to a National Instruments cRIO. A block diagram of the final system is shown in Figure 14.

Figure 14 Location

A STMicroelectronics STM32M4 was selected as the microcontroller in the ARM. It belongs to the System on a Chip (SoC) family of 32-bit microcontrollers with integrated circuits. It is maxed out at a clock frequency of 180 MHz and consists of the processor core, static RAM, flash memory, a debugging interface, and various peripherals.

The incoming signal is filtered, then sent to the low and high gain amplifier sections via two on-board Analog-to-Digital Converters (ADCs). Beam can only occur during the beam gate, so the ARM only samples during beam gates. The system is designed for repetition rates ranging from 1 – 120 Hz. During the beam gate, all interrupts and other tasks are disabled so the ARM can dedicate every available clock cycle to gathering samples. Mathematical operations are performed on the collected data between beam gates. Since the lowest repetition rate is 1 Hz, data is updated and sent out once per second.

To mitigate the effect of noise induced through converting the digital data of the Nuclear Instrumentation Module (NIM) bin to an analogue signal and then having it read back by the control system, a Manchester encoding (also known as phase encoding) unidirectional data stream scheme was

implemented, but any number of protocols could have been used [10]. This enables digital transmission of data from the low current measurement card into a binary module of the control system for decoding and maintains the high accuracy of the measured signal acquired by the low current measurement NIM module.

The analog and digital portions of the circuit were laid out on a single printed circuit board (PCB) to fit a NIM module form factor. The device is calibrated using a Berkeley Nucleonics Corporation 577 function generator and a Keithley 6221 current source.

With this upgraded system, beam current monitoring on the time scale of seconds is now possible with 1% accuracy or better at beam currents down to 100 nA, allowing for precise beam current measurements from very low currents needed for experimental irradiations to the orders of magnitude higher nominal production currents.

4.4 Beam Energy Measurements (Time of Flight)

Approximately 125k micropulses make up each 625 μs macropulse delivered to IPF. By tracking a single micropulse and the time it takes to pass from one Beam Position and Phase Monitor (BPPM) location to another it is possible to determine the proton beam energy. Prior to the AIP there was no automated independent measurement of the incident proton energy. The time of flight measurements are taken by using the BPPM readings at three separate locations. Two of the existing BPPMs (BPPM 04 and 08) were used and a third BPPM (BPPM 07) was added to provide increased resolution. The locations of the BPPMs along the IPF beamline are shown in Figure 15.

Figure 15 Location

The electronics system that has been developed to read out the BPPM data uses a high-speed digitizer coupled with a Field Programmable Gate Array (FPGA) mounted in a VPX chassis that is capable of measuring the position, phase, and bunched-beam current of the IPF beam. The architecture of this system is shown in Figure 16. The system captures signals from four electrodes from each BPPM along with the accelerator reference signal and these signals are conditioned to 201.25 MHz RF waves. The five signals are then digitized and analyzed by a Digital Signal Processor (DSP) to convert waveforms to position, phase, and bunched-beam current. The phases are measured with a precision of less than 0.25°. Using this phase measurement rather than a time-domain approach allows a high precision time of flight measurement that is easily automated [11].

Figure 16 Location

The beam energy, or time of flight, monitoring system takes advantage of the different path lengths between the three BPPMs to achieve the optimum spacing for energy measurement and obtain 50 keV energy resolution. The short paths allow a rough estimate of energy without ambiguity in the integer number of cycles of the 201.25 MHz signal, while the long paths provide high precision. As part of the IPF AIP, measuring the different beam energies at 41, 73, and 100 MeV is now possible. The energy resolution for each beam energy is shown as a function of BPPM spacing in Figure 17, highlighting the usefulness of the three different time of flight (ToF) measurement locations and path lengths and how they allow all three energies to be obtained with 50 keV resolution.

Figure 17 Location

The five waveforms – four electrodes and the reference – are digitized at a rate of 240 Msamples/second, and several samples compose a record that is analyzed to produce phase and amplitude values. For IPF a typical record length is 1 μs (240 samples), but the system can use record lengths between 20 ns and 68 μs. The 1 μs record provides excellent precision while allowing one to see variation on short time scales.

The FPGA is being used for the DSP to analyze these signals in different timing modes such as long pulse (50 μs), short pulse (150 ns), and single shot (1 ns). A soft core processor, which resides in the

FPGA, is used to store the results in a database for use by beam operators and other users. Timing for synchronous measurements between BPPMs and beam specific information is provided by an event receiver connected to the accelerator master timer via optical links. The BPPM results are then stamped with the timing information. A real-time operating system is used to collect data and match it with the correct timing information for each cycle of the beam. An example output of this system is shown in Figure 18. The perturbations seen are within the expected deviation.

Figure 18 Location

In addition to the beam energy measurement provided by three of the BPPMs, they are also able to provide an analysis of the beam centroid as it is rastered with a time resolution of 1 μs and a position resolution of 10 μm. The three BPPM locations allow for tracking of the circle raster pattern as it approaches the IPF target.

This capability has not yet been validated for the 41 and 73 MeV proton beam energies. Since the installation of this system, the accelerator has not been operated at these energies as this impacts the operation of other facilities at LANSCE, but will be validated when opportunity is available.

Figure 19 shows the circle raster pattern for a 2 minute period of time, collapsed into two dimensions in the vertical and horizontal directions. This displayed time-lapse measurement verifies the reproducibility of beam positioning near the target.

Figure 19 Location

The combination of the BPPMs and the upgraded performance of the beam current monitors enables improved calculation of beam power density for enhanced thermal modeling. It also verifies in real time that the beam centroid incident on the target is as expected.

The improved diagnostic beam monitoring capability ensures that the beam profile, current, and incident proton energy are well characterized, enhancing target survivability at higher operating beam currents and potentially increasing the lifetime of future beam window designs by years. Historically there has been no routine, automated, and precise independent measure of incident beam energy, highlighting the significant advances afforded by the AIP.

Post commissioning, the capability facilitated by these upgrades has been demonstrated both by implementation of beam energy measurement capabilities and increased accuracy in the recorded beam current for both routine and high fidelity experimental irradiations.

5 ACTIVE AND ADJUSTABLE COLLIMATOR

An active and adjustable collimator installed as part of the AIP replaced the existing fixed passive collimator. The new collimator is the first of its kind in the world. It consists effectively of two collimators, with eight graphite collimator segments in total – four fixed and four adjustable. Each collimator segment covers approximately a 100 degree angle, with a water-cooled cold plate on the downstream end. The 100 degree angular dimension ensures overlap between the segments. Two collimator segments are installed together in one assembly, with the second assembly of collimator segments rotated by 90 degrees to provide the required 360 degrees of collimation [12].

This orientation for both the fixed and adjustable collimator assemblies is shown in Figure 20.

Figure 20 Location

While the main functionality of a typical collimator is to stop any errant beam, the active components of the new collimator provide feedback on both beam current spill and temperature for each collimator segment. This translates into a real-time characterization of beam quality and position as it enters the IPF target region.

All collimator segments are attached to an electrically isolated water-cooled cold plate, as shown in Figure 21. The cold plate has an internal cooling water channel with a design flow rate of 36 mL/s to provide necessary thermal management. A layer of Shapal^{TM}, was placed between the cold plate and the graphite collimator segment. Shapal^{TM} is a machinable ceramic with a good thermal conductivity and it provides electrical isolation while still facilitating thermal coupling between the cold plate and the graphite.

The graphite-Shapal^{TM}-cold plate assembly is soldered together and additionally secured by stainless steel screws with Macor (machinable glass ceramic) inserts and washers to maintain the required electrical insulation.

Figure 21 Location

Fixed collimator segments are located upstream of the adjustable collimator segments to provide protection of sensitive components when the adjustable segments are moved to larger aperture sizes. This is in addition to a guard ring further upstream that provides additional protection.

This guard ring was present in the previous collimator system, but the design was modified to accommodate the increased collimator aperture and necessary wire routing. The inner diameter of the guard ring was increased to reduce the total incident beam hitting the guard ring when operating at larger rastered beam diameters. In addition, the plate thickness was reduced to allow the 41 MeV beam to exit the guard ring stack and reduce the overall power deposited by the impinging beam (this issue was not considered in the original guard ring design). The modified design also includes design points for the active and adjustable collimator translation straps and necessary electrical wire routing, as seen in Figure 22. The water tubing used for thermal management feeds into and out of the segments for constant water flow, as is additionally illustrated in Figure 23.

Figure 22 Location

The entire collimator assembly shown in Figure 22 fits inside a tube of 12.5 cm inner diameter and is approximately 2 m in length. The collimator aperture size can be changed remotely from a minimum aperture diameter of ~3.56 cm (1.4 in) to a maximum of ~5.84 cm (2.3 in). The aperture dimension is changed via symmetric radial movement of the collimator segments attached to a titanium flexure mechanism. The flexures were constructed using 6Al-4V titanium, and no radiation hardening estimates were performed as it was not considered a concern during the 10 year design life of the collimator. A radiation hardened stepping motor moves these flexure collimator translation strap mechanisms, which make up part of the actuation system. The adjustable collimator assembly is shown in Figure 23, with each component labeled. The actuation system, though not shown in this image, is connected via the strap clamp, which is shown.

This flexure mechanism was determined to be preferable in terms of overall performance to a mechanical linkage due to a longer life expectancy resulting from the smaller total size, repeatability of motion, predictable positioning, and frictionless movement. Pulling the flexure mechanism out all the way closes the collimator segments to their smallest aperture size. Pushing the collimator flexure mechanism brings the collimator segments out to their largest aperture location.

Figure 23 Location

To examine the performance of this system before implementation, both a computational model and an experimental testing prototype were developed.

MCNP was used to generate volumetric heating profiles and ANSYS CFX was used to perform a thermal hydraulic analysis [3,4]. These simulations were used to predict the performance of the cooling system and the temperature profile in the graphite collimator segments under various heat loads up to 500 W.

A review of beam trip data for the LANSCE accelerator indicates up to 1000 beam trips per year of a duration greater than the 8 second thermal time response constant of the collimator. For a practical endurance test, the beam heating was simulated with 4 rod heaters inserted into the graphite of the prototype with uniform heating loads. Assuming a 10 year service life, thermal cycling tests were performed at 10,000 cycles of 100 W, and 100 cycles at the 500W beam tuning maximum heat load.

The peak temperatures seen in this 500 W heat load 100 cycle experimental test and in the corresponding simulation are well below the safe use temperature for the most limiting material – the solder – of 190 °C and its melting point of 212 °C. The conclusion of this study was that there was no expectation of problems arising from beam trip events and that the new collimator system should be more than capable of handling worst-case scenario events.

The active feature of the collimator promotes a reduced risk of target failure due to issues with the incident beam. The temperature and beam current measurements on the collimator segments ensure that the beam profile is correct when entering IPF and beam spill is minimized.

The collimator segments were all equipped with a thermocouple inserted 1.25 cm deep into the graphite on the cooled (downstream) side. The thermocouple is a mineral insulated sheathed probe, entering the graphite through a hole in the cold plate and the Shapal™. The probe sheath is interrupted by a short section of bare wire insulated with Macor beads and then transitions back to a mineral insulated thermocouple wire before running down the vacuum tube to a feedthrough.

A current and temperature screen was developed to allow for real time visualization of the beam current spill and temperatures on each of the collimator segments at IPF. This screen output is shown below in Figure 24.

Figure 24 Location

The new collimator design allows for an increase in production capacity with the maximum aperture setting when coupled with larger target diameters and the more uniform heat distribution provided by the upgraded raster system. It also allows for the flexibility needed for precise tailoring of target diameters for R&D experimental irradiations, e.g. to improve radiochemical separations or reduce target costs. The functionality of the collimator over the designed range was confirmed by performing a series of short irradiations of plastic foils at different collimator settings to ensure functionality over the full range. The performance of the collimator was exercised during the successful 300 μA irradiation of a large 6.35 cm (2.5 in) diameter RbCl/RbCl/Ga target stack at the largest ~5.84 cm (2.3 in) aperture setting.

6 VALIDATION

After commissioning, the upgrades to the IPF beam delivery system were tested and documented to assess performance.

Monitoring the behavior of the beam window via displacement measurements after both of the past two run cycles has indicated that this new beam window design outperforms its predecessor due to the lower thermal stresses imposed by its reduced thickness and a decrease in deformation due to its preformed curvature.

The more uniform power distribution provided by the multi-circle raster has enabled higher beam current on target for a variety of production and research irradiations. Most routine production target stack irradiations are now conducted with a three-circle raster and at a nominal beam current of 250 μA, which is an ~8.7% increase from the pre-AIP production current of 230 μA. The superior thermal properties of metal targets have facilitated even greater increases, with Rb/Rb/Ga stacks having sustained production irradiations at an average beam current of 265 μA with the use of a three-circle raster pattern. Three separate thorium targets have been bombarded at an average beam current of 250 μA for up to 5 days. The more uniform power distribution obtained with the three-circle raster pattern improves target

thermal performance, providing an increased safety margin. This increased safety margin opens the door for future operation at even higher beam currents.

The adjustable collimator now permits the use of different target diameters, as demonstrated with the irradiation of a RbCl-RbCl-Ga large 6.35 cm (2.5 in) diameter target stack. The largest collimator aperture diameter setting was used in conjunction with a five-circle raster pattern to successfully irradiate this target stack at an average beam current of 300 μA for a 24 hour period. Historically, the maximum allowable beam current on the smaller 5.08 cm (2 in) diameter RbCl targets was 230 μA due to observed failures at currents higher than this. Safe operation at a production beam current of 300 μA provides a ~30% increase in production capacity compared with the historical 230 μA nominal beam current allowed on typical RbCl production targets. Successful irradiation at this increased average beam current provides strong evidence for the long term survivability of these larger diameter targets for future production runs. When these targets were processed to verify yields, the appreciable increase in ^{68}Ge and ^{82}Sr production yields proportional to the increase in beam current was evident.

In all production and R&D runs, the diagnostic equipment implemented during the AIP provided quality control through visualization of the beam shape and location with the high density harp and a more reliable estimate of the beam current and energy incident upon the target stack with the improved diagnostic capabilities. This more accurate diagnostic equipment facilitated a high fidelity R&D experiment for the measurement of proton induced cross sections in lanthanum at a beam current of 100 nA. Historically, the large uncertainties in the beam current measurement below ~500 nA would have been prohibitive to obtaining an independent measure of beam current. The upgrades to the beam diagnostic capabilities have allowed the flexibility to operate over an extremely wide range of beam currents and characterize the instantaneous beam current with an accuracy of 1% down to a beam current of 100 nA.

7 CONCLUSIONS

As demonstrated by recent landmark production and experimental runs discussed above, the technical advances made during the Accelerator Improvement Project (AIP) have significantly increased the operating capability and reliability of IPF.

These upgrades support a cumulative theoretical increase in isotope production capacity by a factor of up to ~1.96 when combining the increase in production capacity obtained by using the largest collimator aperture size and the higher beam currents up to 450 μA achievable with the new raster improvements. However, these upgrades also allow for the flexibility necessary to tailor irradiations to meet specific production or R&D needs. It is anticipated that these advances will greatly benefit future operations at IPF, allowing for variable target diameters and higher beam currents to enhance production capacity and increase flexibility for research, and improve reliability with robust and accurate beam diagnostics.

8 ACKNOWLEDGEMENTS

This work was supported through an Accelerator Improvement Project from the U.S. Department of Energy Isotope Program, managed by the Office of Science for Nuclear Physics.

The LANL Accelerator Operations and Technology (AOT) division at LANL is gratefully acknowledged for their division wide effort to successfully complete these upgrades.

The Isotope Production Team at LANL is gratefully acknowledged for the target irradiation and yield information.

9 REFERENCES

[1] K.F. Johnson, H. Alvestad, W. Barkley, D. Barlow, D. Barr, G. Bennett, L. Bitteker Jr, E. Bjorkland, W. Boedeker, M. Borden, R. Cardon, G. Carr, J. Casados, S. Cohen, J. Cordova, J. Faucett, M. Fresquez, F. Gallegos, J.D. Gilpatrick, F. Gonzales, F. Gorman, M. Gulley, M. Hall, D. Hayden, R. Heaton, D. Henderson, D. Ireland, E. Jacobson, G. Johns, D. Kersteins, A. Maestas,

A. Martinez, D. Martinez, G. Martinez, J. Martinez, M. Martinez, R. Merl, J. Merrill, B. Meyer, R. Meyer Sr, M. Milder, E. Morgan, M. Nortier, J. O'Hara, F. Olivas, M. Oothoudt, T. Pence, M. Perez, E. Peterson, C. Pillai, F. Romero, C. Rose, L. Rybarcyk, G. Sanchez, J. Sandoval, S. Schaller, F. Shelley Jr, R.B. Shurter, W. Sommer, M. Stettler, J. Stockton, J. Sturrock, T. Tomei, F. Valdez, V. Vigil, P. Walstrom, P. Wanco, J. Wilmarth, Commissioning and Initial Operation of the Isotope Production Facility at the Los Alamos Neutron Science Center (LANSCE), in: Proc. EPAC 2004, Lucerne, Switzerland, 2004: pp. 2816–2818.

[2] H.T. Bach, O. Anderoglu, T.A. Saleh, T.J. Romero, C.T. Kelsey, E.R. Olivas, B.H. Sencer, P.O. Dickerson, M.A. Connors, K.D. John, S.A. Maloy, Proton irradiation damage of an annealed Alloy 718 beam window, J. Nucl. Mater. 459 (2015) 103–113. doi:10.1016/j.jnucmat.2014.12.096.

[3] MCNPX, (2008).

[4] ANSYS, ANSYS CFX, Release 16.0, (2016).

[5] ANSYS, ANSYS Mechanical, Release 16.0, (2016).

[6] M. Pieck, S. Baily, E. Espinoza, J. Faucett, J. Hill, F.M. Nortier, J.F.O. Hara, E.R. Olivas, A.R. Patten, L. Rybarcyk, J. Snyder, E.A. Swensen, R. V Valicenti, H.A. Watkins, K. Woloshun, Recent Enchancements to the Los Alamos Isotope Production Facility, in: Proc. 16th Int. Conf. Accel. Large Exp. Control Syst., JACoW Publishing, Barcelona, Spain, 2017: pp. 548–552. doi:10.18429/JACoW-ICALEPCS2017-TUPHA065.

[7] H. Watkins, D. Baros, D. Martinez, L. Rybarcyk, J. Sedillo, R. Valicenti, Upgrades to the LANSCE Isotope Production Facilities Beam Diagnostics, in: Proc. IBIC2016, Barcelona, Spain, 2016: pp. 690–693.

[8] J. Sedillo, D. Baros, J. O'Hara, L. Rybarcyk, R. Valicenti, H. Watkins, LANSCE Isotope Production Facility Emittance Measurement System, in: Proc. IBIC2016, Barcelona, Spain, 2016: pp. 548–550.

[9] M.G. Minty, F. Zimmermann, Measurement and Control of Charged Particle Beams, Springer, 2003.

[10] R. Forster, Manchester encoding : opposing definitions resolved, Eng. Sci. Educ. J. 9 (2000) 278–280. doi:10.1049/esej:20000609.

[11] R.C. Mccrady, H.A. Watkins, Signal Processing Algorithm for Beam Position and Phase Monitors at LANSCE, in: Proc. IBIC2015, Melbourne, Australia, 2015: pp. 540–541.

[12] K. Woloshun, J. O'Hara, E. Olivas, A. Maestas, E. Swensen, H. Salazar, A Water Cooled, Active and Adjustable Aperture Collimator, in: Proceeding 13th Intern. Top. Meet. Nucl. Appl. Accel., Quebec City, Quebec, 2017: pp. 316–325.

Journal Pre-proof

Journal Pre-proof

Figure 1

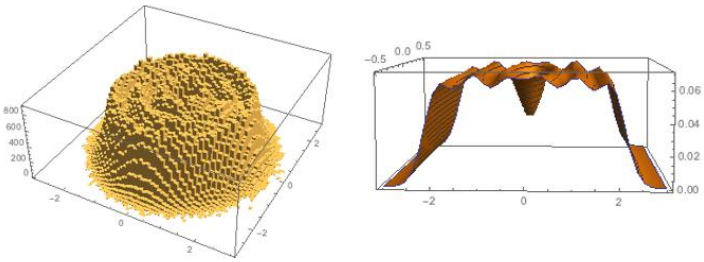

Figure 1. Distribution of three-circle rastered beam (left) and central slice (right) with a 5.84 cm (2.3 in) diameter aperture size used to generate a power distribution in MCNP.

Journal Pre-proof

Journal Pre-proof

Figure 2

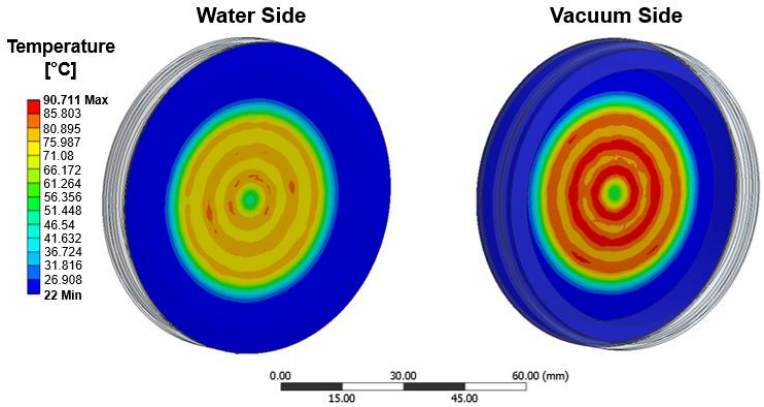

Figure 2. Temperature profile of the beam window-water (left) and beam window-vacuum (right) interfaces of the 0.381 mm thick beam window with a 5.84 cm (2.3 in) collimator aperture size and 100 MeV, 450 μA incident proton beam. *Color online.*

Journal Pre-proof

Journal Pre-proof

Figure 3

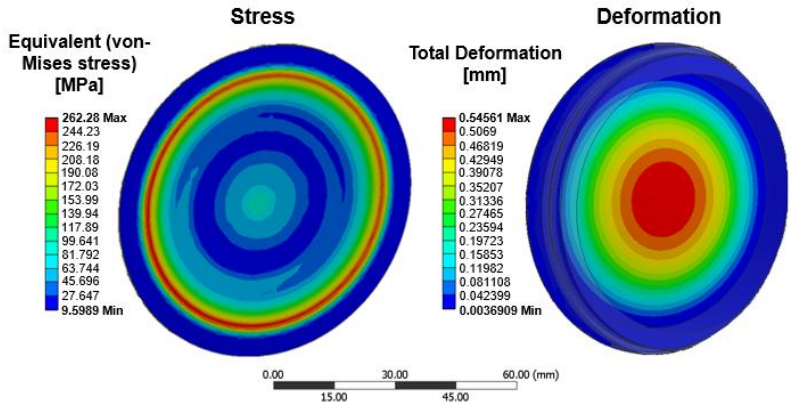

Figure 3. Stress (left) and deformation (right) profiles in the 0.381 mm thick beam window with a 5.84 cm (2.3 in) collimator aperture size and 100 MeV, 450 μA incident proton beam. *Color online.*

Journal Pre-proof

Journal Pre-proof

Figure 4

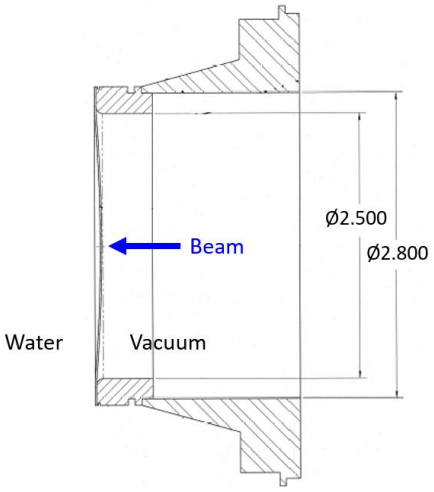

Figure 4. Drawing of new preformed IPF beam window and assembly.

Journal Pre-proof

Journal Pre-proof

Figure 5

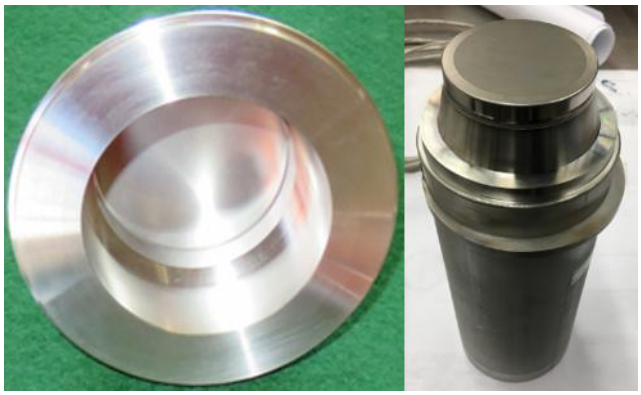

Figure 5. IPF beam window and weld flange (left) and full beam window assembly (right).

Journal Pre-proof

Journal Pre-proof

Figure 6

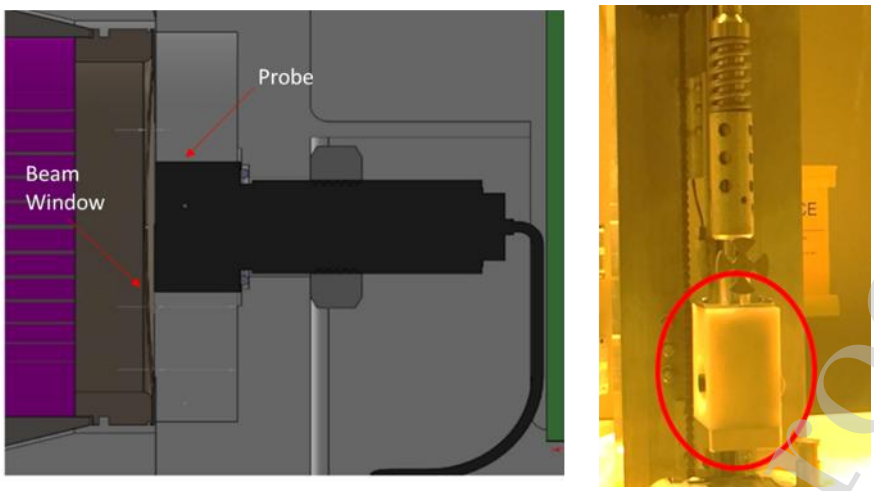

Figure 6. Model of beam window displacement apparatus assembly in the IPF docking station (left) and beam window displacement housing attached to the IPF trolley (right).

Journal Pre-proof

Journal Pre-proof

Figure 7

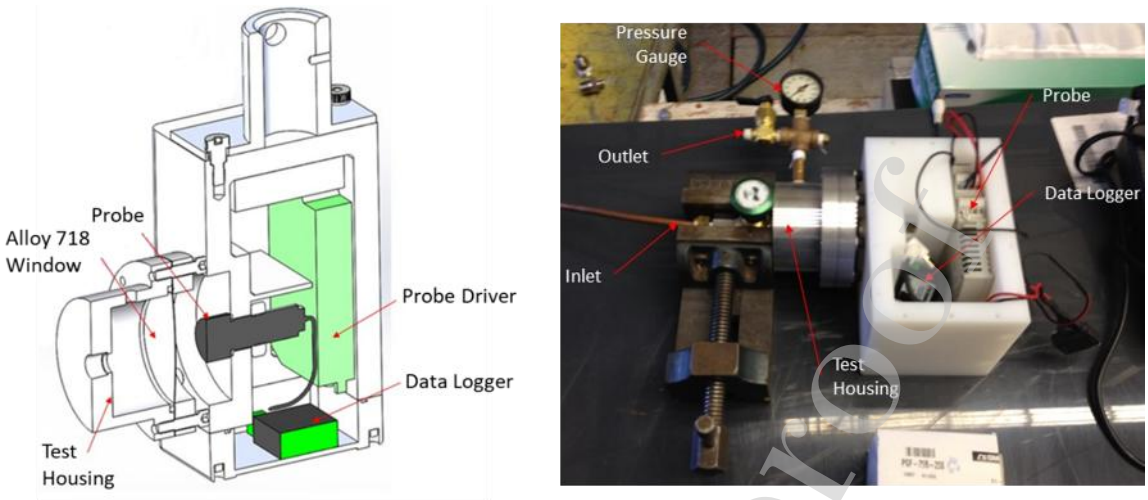

Figure 7. CAD geometry (left) and experimental set up (right) benchtop testing apparatus used to measure beam window deformation under different loading conditions.

Journal Pre-proof

Journal Pre-proof

Figure 9

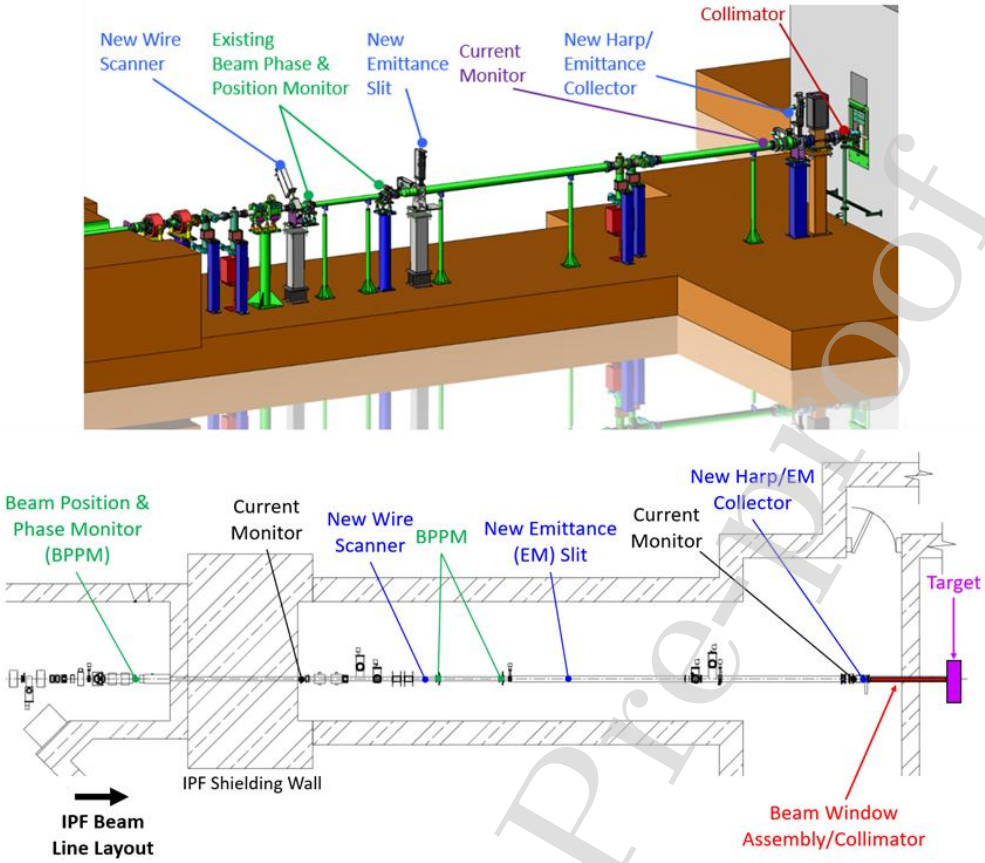

Figure 9. Three-dimensional model (top) and two-dimensional drawing (bottom) of the IPF beamline with locations of new or upgraded beam diagnostics. *Figure should span full page width.*

Journal Pre-proof

Journal Pre-proof

Figure 8

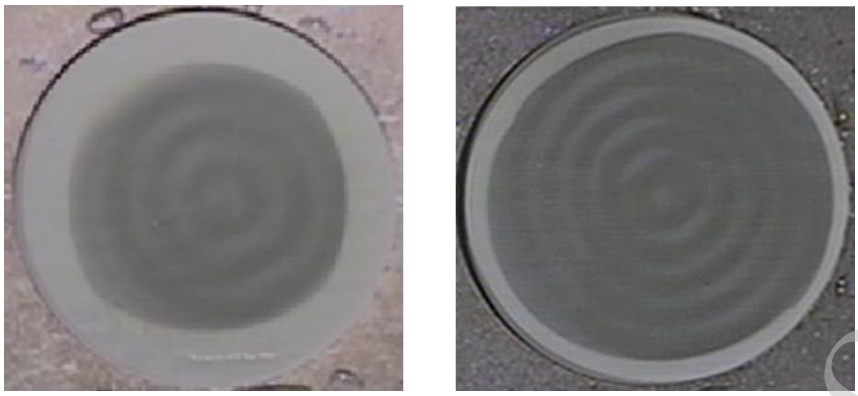

Figure 8. Burn marks on a polymer film with a three-circle raster pattern and 4.57 cm (1.8 in) aperture size (left) and with a five-circle raster pattern and 5.84 cm (2.3 in) aperture size (right), with the raster circles denoted by the darker burn marks.

Journal Pre-proof

Journal Pre-proof

Figure 10

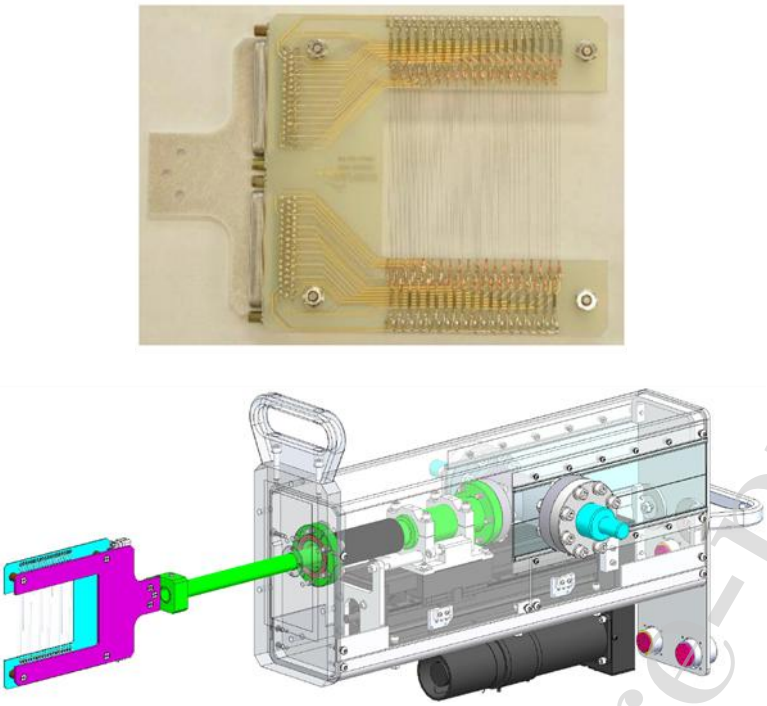

Figure 10. Harp head assembly (top) and harp and actuator three-dimensional CAD model (bottom).

Journal Pre-proof

Journal Pre-proof

Figure 11

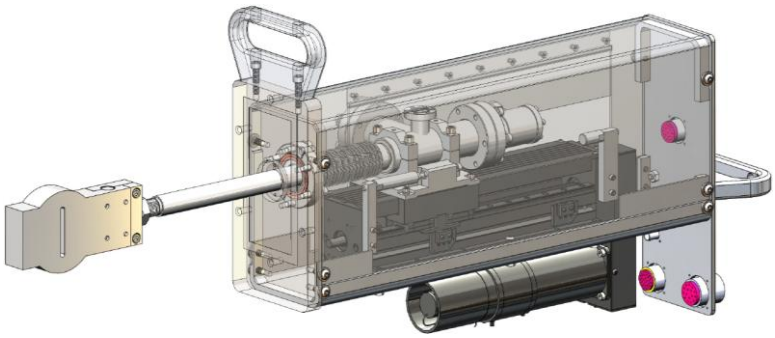

Figure 11. Emittance slit and actuator three-dimensional CAD model.

Journal Pre-proof

Journal Pre-proof

Figure 12

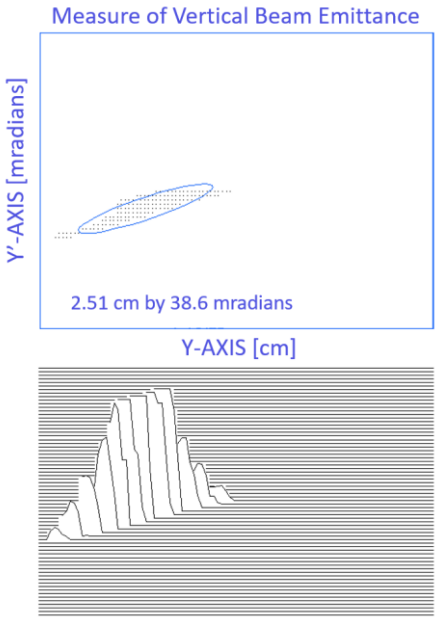

Figure 12. Two-dimensional (top) and three-dimensional (bottom) measurement of vertical IPF beam emittance, or phase-space area, using the new high-density harp and emittance slit system.

Journal Pre-proof

Journal Pre-proof

Figure 13

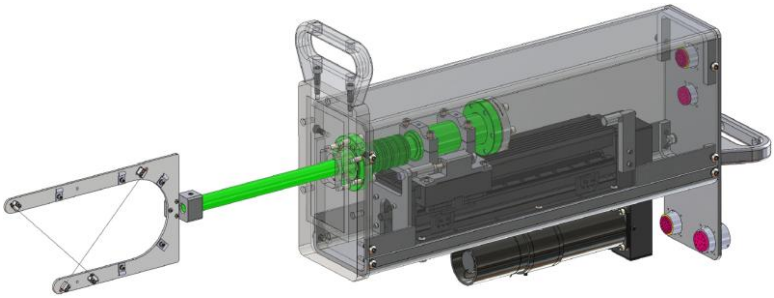

Figure 13. Three-dimensional CAD model of the wire scanner and actuator assembly.

Journal Pre-proof

Journal Pre-proof

Figure 14

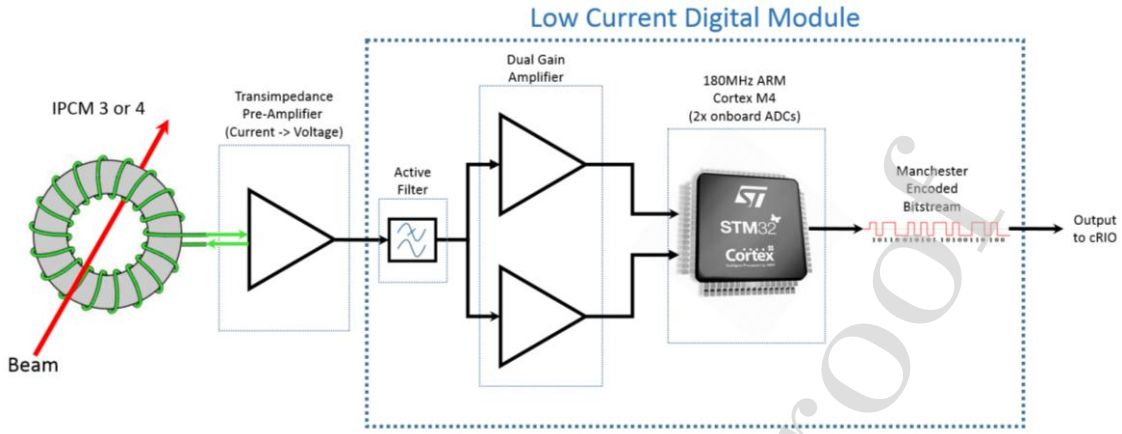

Figure 14. Low current measurement system block diagram.

Journal Pre-proof

Journal Pre-proof

Figure 15

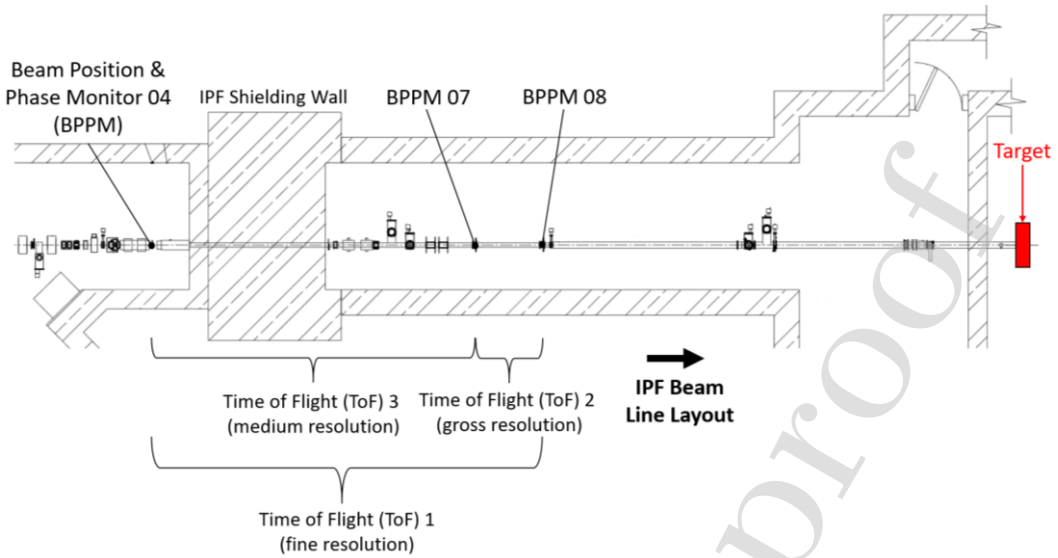

Figure 15. IPF beamline layout with Beam Position and Phase Monitors (BPPMs) used for the beam energy measurements. *Figure should span full page width.*

Journal Pre-proof

Journal Pre-proof

Figure 16

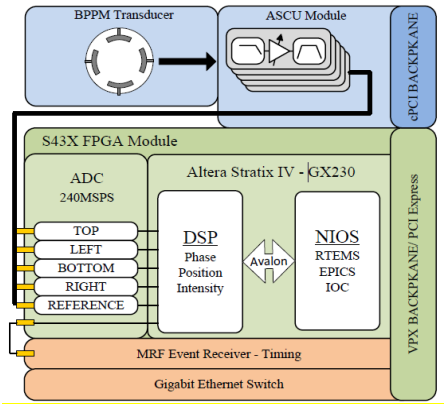

Figure 16. BPPM data acquisition system architecture.

Journal Pre-proof

Journal Pre-proof

Figure 17

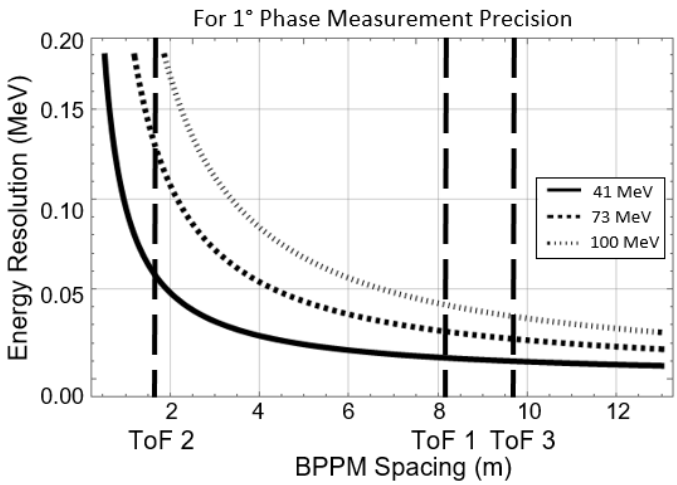

Figure 17. Energy resolution for different beam energies as a function of BPPM spacing.

Journal Pre-proof

Journal Pre-proof

Figure 18

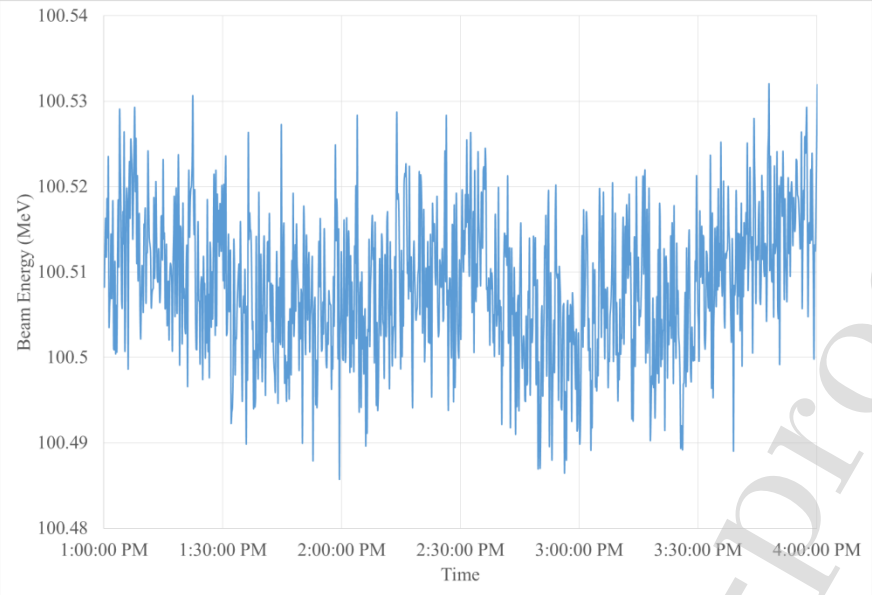

Figure 18. Beam energy (100 MeV range) versus time measurements using the new data acquisition system.

Journal Pre-proof

Journal Pre-proof

Figure 19

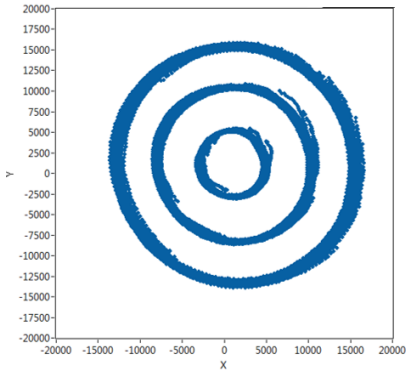

Figure 19. Three-circle raster pattern in vertical and horizontal dimensions (µm) collapsed over a 2 minute time period.

Journal Pre-proof

Journal Pre-proof

Figure 20

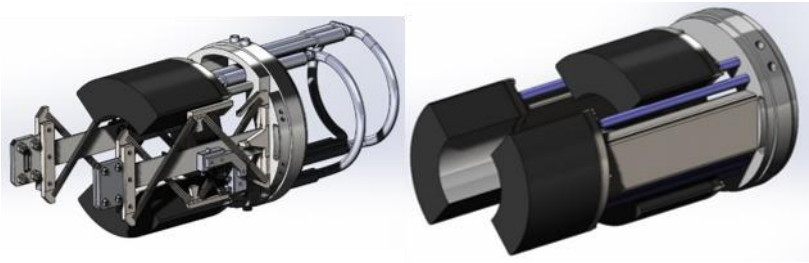

Figure 20. One half of flexible (left) and complete fixed (right) collimator assemblies.

Journal Pre-proof

Journal Pre-proof

Figure 21

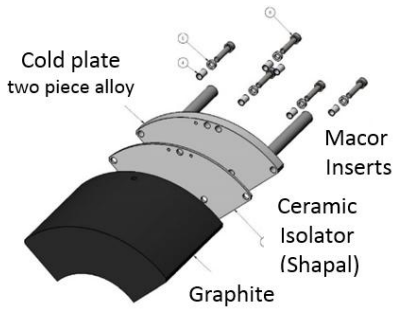

Figure 21. Single graphite collimator segment with attached cold plate assembly.

Journal Pre-proof

Journal Pre-proof

Figure 22

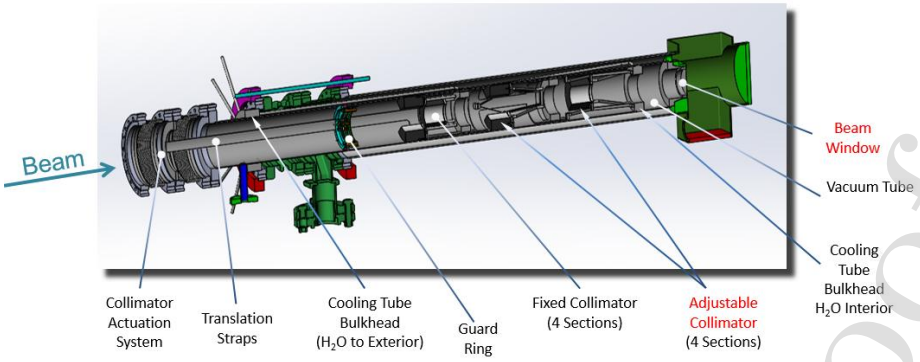

Figure 22. Vacuum tube and collimator assembly components.

Journal Pre-proof

Journal Pre-proof

Figure 23

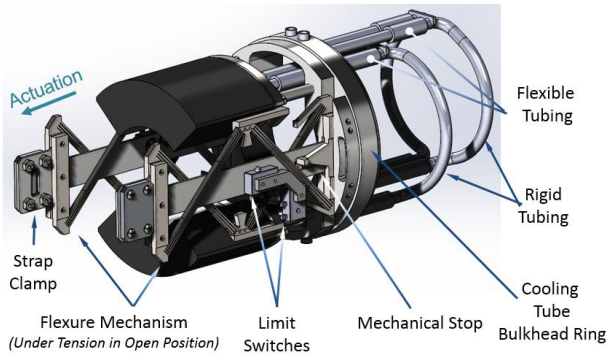

Figure 23. Adjustable collimator assembly and actuation system.

Journal Pre-proof

Journal Pre-proof

Figure 24

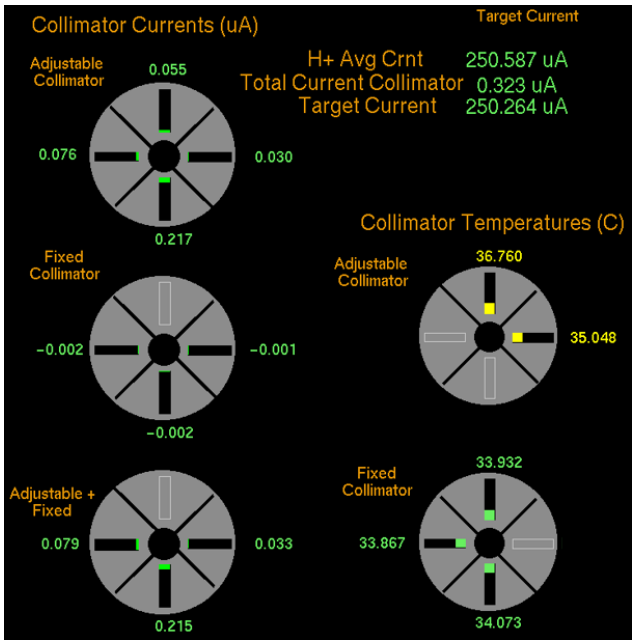

Figure 24. Control panel showing the adjustable, fixed, and combined collimator beam current readouts (left) and adjustable and fixed collimator thermocouple readouts (right).

Journal Pre-proof

Journal Pre-proof

***Declaration of Interest Statement**

Declaration of interests

☒ The authors declare that they have no known competing financial interests or personal relationships that could have appeared to influence the work reported in this paper.

☐The authors declare the following financial interests/personal relationships which may be considered as potential competing interests:

Journal Pre-proof